

THE RARE EARTH PEAK: AN OVERLOOKED r -PROCESS DIAGNOSTIC

MATTHEW R. MUMPOWER¹, G. C. MCLAUGHLIN¹, AND REBECCA SURMAN²

¹ Department of Physics, North Carolina State University, Raleigh, NC 27695-8202, USA; mrmumpow@ncsu.edu, gail_mclaughlin@ncsu.edu

² Department of Physics and Astronomy, Union College, Schenectady, NY 12308, USA; surmanr@union.edu

Received 2012 February 8; accepted 2012 April 15; published 2012 June 4

ABSTRACT

The astrophysical site or sites responsible for the r -process of nucleosynthesis still remains an enigma. Since the rare earth region is formed in the latter stages of the r -process, it provides a unique probe of the astrophysical conditions during which the r -process takes place. We use features of a successful rare earth region in the context of a high-entropy r -process ($S \gtrsim 100k_B$) and discuss the types of astrophysical conditions that produce abundance patterns that best match meteoritic and observational data. Despite uncertainties in nuclear physics input, this method effectively constrains astrophysical conditions.

Key word: nuclear reactions, nucleosynthesis, abundances

Online-only material: color figures

1. INTRODUCTION

Among many open problems in modern nuclear astrophysics, a complete understanding of the rapid neutron capture or “ r -process” remains one of the greatest challenges. The r -process is believed to be responsible for approximately half the heavy elements above the iron group. There are many promising candidate sites for this synthesis process, however the exact astrophysical site has not yet been identified; for reviews see Arnould et al. (2007) and Qian et al. (2007). Some examples of candidate sites include high-entropy supernovae ejecta (Meyer et al. 1992; Qian & Woosley 1996; Sumiyoshi et al. 2000; Thompson et al. 2001), compact object mergers (Lattimer et al. 1977; Meyer 1989; Freiburghaus et al. 1999; Goriely et al. 2005; Surman et al. 2008; Metzger et al. 2010), neutrino induced nucleosynthesis in He shells (Woosley et al. 1990; Banerjee et al. 2011), or possibly γ -ray burst scenarios (Surman & McLaughlin 2004; McLaughlin & Surman 2005; Surman et al. 2006).

The study of the r -process is further complicated by the short-lived nuclides far from stability. Recent experiments have led to measurements on some nuclides participating in the r -process, e.g., Hosmer et al. (2005), Matoš et al. (2008), Rahaman et al. (2008), Baruah et al. (2008), Jones et al. (2009), Hosmer et al. (2010), Nishimura et al. (2011), and Quinn et al. (2011). However current experimental data on neutron-rich isotopes is sparse, see, e.g., Figure 12 in Mumpower et al. (2011). Therefore, theoretical extrapolations must be used as no experimental data are available (Grawe et al. 2007). Much theoretical work is ongoing to understand the properties of nuclei far from stability and their impact on the r -process; see, e.g., Möller et al. (1995), Pearson et al. (1996), Rauscher et al. (1998), Rauscher et al. (2000), Möller et al. (2003), Beun et al. (2008), Surman et al. (2009), Goriely et al. (2009), Mumpower et al. (2011), Arcones & Bertsch (2011), and Suzuki et al. (2012).

Suess & Urey (1956) demonstrated the existence of the $A = 130$ and $A = 195$ peaks in an improved distribution of solar abundances. The prominent abundance features seen in this curve were quickly attributed to closed neutron shells occurring at magic neutron numbers (Burbidge et al. 1957). The rare earth peak ($A \sim 160$), lying away from closed neutron shells, must occur by a different mechanism.

Three mechanisms have been proposed for the formation of the rare earth peak. (1) It has been hypothesized that this peak

may form by fission cycling if the distribution of fission fragments in (A, Z) is favorable (Cameron 1957; Schramm et al. 1971; Marti & Zeh 1985; Goriely 2011). (2) Surman et al. (1997) discovered that the rare earth peak can form during freezeout as material decays back to stability. Crucial to this argument was that this mechanism occurs in a “hot freezeout,” with temperature high enough to support significant photodissociation flow. This allowed material to “funnel” into the peak in an attempt to sustain $(n, \gamma) \rightleftharpoons (\gamma, n)$ equilibrium. Otsuki et al. (2003) found similar abundance patterns provided the temperature was constant during freezeout. (3) A third mechanism has also been found for lower temperature environments where a “cold freezeout” may occur (Mumpower et al. 2011). In this scenario the temperature-dependent photodissociations flow is not present, however the rare earth peak may still form by a trapping mechanism involving slow neutron capture rates in the region. The formation process in addition to being sensitive to freezeout conditions was also shown to be sensitive to nuclear physics inputs (Mumpower et al. 2011; Arcones & Martínez-Pinedo 2011).

One of the most intriguing results to date regarding r -process yields is that the stable elements observed in galactic halo stars (much older than the sun) with $56 \lesssim Z \lesssim 80$, including the rare earth elements ($Z = 57$ to $Z = 71$), are consistent with the scaled solar r -process elemental abundances e.g., see Sneden et al. (1996). This is fascinating because it suggests these elements were formed by an r -process mechanism that operates over a wide range of metallicity, e.g., see Cowan et al. (1997).

An understanding of the production of the rare earth elements can be used to probe the freezeout conditions of the r -process mechanism(s) that operates over a wide range of metallicity. This approach complements previous calculations that have focused on the conditions at the onset of the r -process, i.e., the neutron-to-seed ratio (Hoffman et al. 1997; Meyer & Brown 1997; Freiburghaus et al. 1999).

In this paper, we introduce three new rare earth peak constraints on astrophysical conditions in the context of the site of the r -process. Using the formation of the rare earth peak as our key constraint, we isolate freezeout conditions that are favorable for the production of these elements. We compare final abundances from simulations to both the elemental abundances of halo stars and the isotopic abundances of r -process residuals. It is essential to note that (1) the r -process abundance pattern we

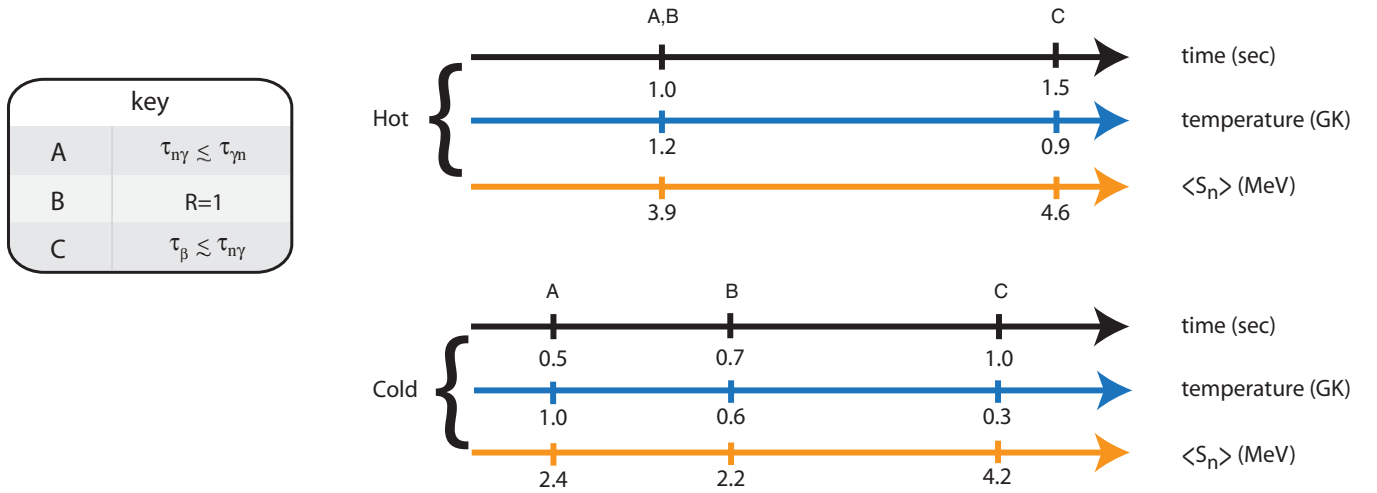


Figure 1. Contrasts the timeline of important events during the formation and evolution of the rare earth region between hot and cold evolutions. Point A represents the beginning of $(n, \gamma) \rightleftharpoons (\gamma, n)$ freezeout, point B neutron exhaustion (neutron-to-seed ratio of unity, $R = 1$), and point C when the timescale for β -decays take over neutron capture.

(A color version of this figure is available in the online journal.)

observe may come about from a superposition of abundance patterns made from different conditions in the same astrophysical environment and (2) there exists significant variation between the final abundances using different nuclear models. We take this into consideration by averaging over and computing the variance of final abundances given different nuclear models and conditions. This allows us to compare final abundances, with error bars, to meteoritic and observational data.

2. r -PROCESS MODEL

Nuclides decay back to stability during freezeout, the last stage of the r -process. To monitor this progress, it is useful to consider abundance-weighted timescales for the primary reaction channels: neutron capture, photodissociation, and β -decay:

$$\tau_{n\gamma} \equiv \frac{\sum_{Z \geq 8, A} Y(Z, A)}{\sum_{Z \geq 8, A} N_n \langle \sigma v \rangle_{Z, A} Y(Z, A)} \quad (1a)$$

$$\tau_{\gamma n} \equiv \frac{\sum_{Z \geq 8, A} Y(Z, A)}{\sum_{Z \geq 8, A} \lambda_{\gamma n}(Z, A) Y(Z, A)} \quad (1b)$$

$$\tau_{\beta} \equiv \frac{\sum_{Z \geq 8, A} Y(Z, A)}{\sum_{Z \geq 8, A} \lambda_{\beta}(Z, A) Y(Z, A)}. \quad (1c)$$

In Equation (1), the neutron number density is denoted by N_n . The Maxwellian-averaged neutron capture cross section for nuclide (Z, A) is $\langle \sigma v \rangle_{Z, A}$ and $\lambda_{\gamma n}(Z, A)$ the photodissociation rate. The full β -decay rate (including β -delayed neutron emission channels) for nuclide (Z, A) is denoted by $\lambda_{\beta}(Z, A)$ and $Y(Z, A)$ is the abundance of nuclei (Z, A) . A reduced sum over the rare earth peak region ($A = 150$ to $A = 180$), denoted with a superscript “REP,” may be taken when applicable.

The neutron-to-seed ratio or R is another useful metric, we define as

$$R \equiv \frac{Y_n}{\sum_{Z \geq 8, A} Y(Z, A)}, \quad (2)$$

where Y_n is the abundance of free neutrons. We consider “low” neutron-to-seed ratio to be the time after neutron exhaustion or $R = 1$.

The final abundances are highly dependent on the rate of decline in the temperature and density during the last stage of the r -process (Arcones & Martínez-Pinedo 2011; Mumpower et al. 2011). Among many possibilities, two thermodynamic evolutions are noteworthy and could occur in any astrophysical environment. A “hot” freezeout which proceeds under high temperatures ($T_9 \gtrsim 0.6$) when material decays back to stability and a “cold” freezeout which proceeds under low temperatures ($T_9 \lesssim 0.6$) when material decays back to stability, e.g., Wanajo (2007).

We contrast the differences in the evolution of the rare earth region between the two thermodynamic trajectories in Figure 1. The trajectories used in this figure are from Mumpower et al. (2011) and the values in the timeline represent typical simulations that produce a satisfactory rare earth region compared to the solar isotopic abundances. Figure 2 highlights the free neutron abundance, Y_n , during these calculations and compares them to two more calculations, which include fission. We note that all of the simulations studied here shown qualitatively similar behavior.

The rare earth region typically breaks from $(n, \gamma) \rightleftharpoons (\gamma, n)$ equilibrium at $T_9 \sim 1$, represented by point A in the figure. In the hot evolution, this is due to neutron exhaustion ($R = 1$) while in the cold evolution this is due to the rapidly dropping density. Once the neutron-to-seed-ratio is unity, point B, the rare earth peak may begin to form (Surman et al. 1997; Mumpower et al. 2011). This process usually lasts until β -decays take over neutron captures in the region, point C. However, small changes in the pattern can continue after point C, until $\tau_{n\gamma}^{\text{REP}} \approx$ a few $\tau_{\beta}^{\text{REP}}$ (not shown in the figure). The abundance-averaged neutron separation energy is denoted by $\langle S_n \rangle$. Following this quantity along the timeline, we clearly see the rare earth peak forms as the nuclides decay back to stability (increasing values of $\langle S_n \rangle$) and that cold freezeout calculations typically extend farther from stability, closer to the neutron dripline than hot freezeout calculations. For further discussions of late-time r -process dynamics see Surman et al. (1997), Surman & Engel (2001), Arcones & Martínez-Pinedo (2011), Mumpower et al. (2010), and Mumpower et al. (2011).

In order to probe the conditions that are ideal for the r -process as matter decays back to stability, we study a range

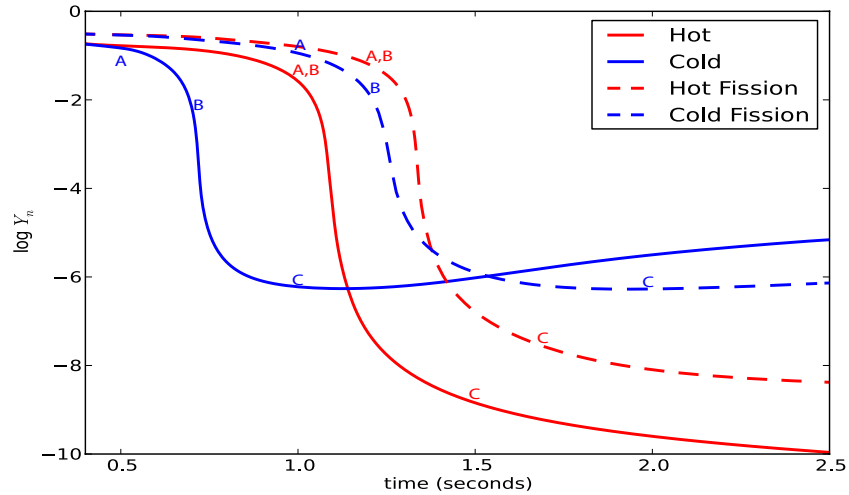


Figure 2. Comparison of the free neutron abundance, Y_n , between differing thermodynamic evolutions. The FRDM nuclear model was used in each calculation. Four evolutions are shown: hot ($n = 2.0$, $S = 200k_B$, $Y_e = 0.30$), cold ($n = 6.0$, $S = 200k_B$, $Y_e = 0.30$), hot fission ($n = 2.0$, $S = 350k_B$, $Y_e = 0.30$), and cold fission ($n = 6.0$, $S = 350k_B$, $Y_e = 0.30$). Points A, B, and C correspond to the important events from the timeline, see previous figure.

(A color version of this figure is available in the online journal.)

of possible outflow parameterizations. Our model consists of a monotonically decreasing temperature with density parameterized as

$$\rho(t) = \rho_1 \exp(-t/\tau) + \rho_2 \left(\frac{\Delta}{\Delta + t} \right)^n. \quad (3)$$

In Equation (3), t denotes simulation time, $\rho_1 + \rho_2$ is the initial density at time $t = 0$, $3\tau = \tau_{\text{dyn}}$ with τ_{dyn} being the dynamical timescale and Δ is a constant real number. For our calculations we take $\tau \sim 27$ ms. The combination of τ and entropy per baryon, S , determines the distribution of seeds and the value of R at the onset of the neutron capture phase. We hold τ constant and vary S in our calculations. The parameter n sets the thermodynamic behavior of the evolution at a low neutron-to-seed ratio. A hot r -process evolution has typical values of $n \sim 2$, which is characteristic of wind models (Meyer 2002; Panov & Janka 2009). Values of $n \gtrsim 5$ are typical of cold r -process evolutions and correspond to a faster decline (Wanajo 2007).

Our r -process calculations are conducted with a nuclear reaction network that includes approximately 4000 nuclides relevant to the r -process. This code is fully dynamic in the sense that it does not assume any equilibrium conditions. The initial abundances for these nuclides are taken from an intermediate reaction network (Hix 1999) with PARDISO solver (Schenk & Gärtner 2004). During the decay back to stability the primary reaction channels are neutron capture, photodissociation, beta-decay, beta-delayed neutron emission, spontaneous fission, and beta-delayed fission.

Asymmetric fission is included during these freezeout calculations (Seeger et al. 1965) and operates for entropies above $S = 200k_B$ with proton to nucleon ratio or electron fraction, $Y_e = 0.30$ and above $S = 300k_B$ with $Y_e = 0.40$. However, in these calculations, fission is not particularly important to the abundances at or above the atomic mass range of the rare earth peak until $S \sim 275k_B$ for $Y_e = 0.30$ and $S \sim 375k_B$ for $Y_e = 0.40$.

To account for uncertainties in nuclear physics our nucleosynthesis calculations use three different nuclear data sets: Finite Range Droplet Model (FRDM; Möller et al. 1995; Rauscher et al. 2000, 1998), Extended Thomas-Fermi with Strutinsky

Integral and Quenching (ETFSI-Q; Pearson et al. 1996; Rauscher et al. 2000, 1998), and version 17 of the Hartree Fock Bogoliubov model (HFB-17; Goriely et al. 2009, 2008).³ We note that the β -decay rates used for our calculations are only consistent with the FRDM nuclear data set. Since we arrive at our main conclusions after taking averages over and variances due to differences in nuclear models, we expect relatively small quantitative changes in our results from this approximation. However, caution is warranted when attempting to judge the validity of individual nuclear models. The consistency of nuclear data for nuclear astrophysics investigations remains the subject of future research.

3. COMPARING SIMULATIONS TO DATA

In this section, we compare final abundances to both halo star and solar data. We now comment on each of these data sets.

Spectroscopic observations of galactic halo stars are useful in learning about the nature of nucleosynthesis processes that occur early in the history of the galaxy; see Sneden et al. (1996), and references therein. The consistency of the rare earth elemental abundance data among metal-poor halo stars is quite remarkable. This evidence suggests that these elements were synthesized in the same type of synthesis event (Sneden et al. 2008) and by a mechanism that operates over a wide range of metallicity, for review see Cowan & Sneden (2006). Early galactic halo stars also provide an important diagnostic for r -process models as the s -process, occurring primarily in lower mass asymptotic giant branch stars, is not believed to have occurred yet.

We compare simulations to an averaged data set of five r -process rich halo stars: CS22892-052 (Sneden et al. 1996), CS31082-001 (Hill et al. 2002), HD115444 (Westin et al. 2000), HD221170 (Ivans et al. 2006), and BD+17°3248 (Cowan et al. 2002). This averaged data set represents a typical r -process rich halo star. Before averaging the halo star data we arbitrarily normalized each halo star data to $\log \epsilon(Z = 63) = 0$. We note that this choice of scaling is not critical to the analysis and has been used elsewhere in the literature, e.g., in Roederer et al.

³ <http://www.astro.ulb.ac.be/>

(2010). We denote the averaged halo star elemental abundances as $H(Z)$.

The solar isotopic abundance pattern corresponds to a superposition of many different events before the origin of the solar system (Kappeler 1989; Arlandini 1999; Cowan & Sneden 2006; Lodders et al. 2009). A further complication arises when using solar data because in order to extract the solar r -process residuals, s -process components must be known accurately (Kappeler 1989; Arlandini 1999; Roederer et al. 2010). Despite these intricacies, solar r -process elemental yields for the rare earth region are strikingly similar to the elemental abundances of metal-poor, r -process rich halo stars. This means that solar data can also be used to constrain favorable freezeout conditions with the additional advantage of isotopic information.

In the follow analysis we use the most recent solar data from Lodders et al. (2009). This data set contains accurately measured abundances among the rare earth elements. To obtain r -process residuals, $N_{\odot,r}$, we take this solar data and subtract from it the stellar model s -process abundances from Arlandini (1999). The r -process residuals, $N_{\odot,r}$, are in good agreement with previous data sets (Kappeler 1989; Arlandini 1999).

3.1. Definitions

In this Section 3.1, we introduce a series of definitions that we use in the remainder of Section 3 to compare simulation to data.

To compare simulations to halo star abundance data, $H(Z)$, we first perform individual calculations using the three nuclear data sets (FRDM, ETFSI, and HFB-17) with conditions varying between $0 \leq n \leq 10$, $100k_B \leq S \leq 400k_B$, and with $Y_e = 0.30$ or $Y_e = 0.40$. We then proceed to take an average of the final abundances from simulations over the different nuclear data holding the conditions constant (n , S , Y_e). We then compare (1) element by element the rare earth peak ($A = 159$ to $A = 167$ or $Z = 64$ through $Z = 68$) and (2) the ratio of total abundance in the rare earth peak to the platinum peak ($A = 195$ or $Z = 78$) of the averaged simulation output to the corresponding values of our compiled halo star.

To accomplish the first comparison we use G_Z^{REP} where,

$$G_Z^{\text{REP}} \equiv \frac{\sum_{Z=64}^{Z=68} (\alpha Y(Z) - H(Z))^2}{\sum_{Z=64}^{Z=68} H(Z)^2}. \quad (4)$$

In Equation (4), $Y(Z) \equiv \sum_A Y(Z, A)$ denotes the final abundance of the stable element with proton number Z and $H(Z)$ is the average abundances of the five halo stars for given proton number. The summation is performed only over the rare earth peak elements as highlighted by the superscript ‘‘REP.’’ A lower value of G_Z^{REP} implies a better match, with $G_Z^{\text{REP}} = 0$ representing perfect agreement with $H(Z)$. We scale the final abundance pattern, $Y(Z)$, by α which is the solution to $dG_Z^{\text{REP}}/d\alpha = 0$.

The $A = 195$ peak to rare earth peak ratio is an important second constraint as both the lanthanides and heavier elements are believed to be produced in the same synthesis event and so their ratios must match observational data. We compare the ratio of simulations to $H(Z)$ using η_Z where,

$$\eta_Z \equiv \left| \frac{\alpha Y(Z=78)}{\sum_{Z=64}^{Z=68} \alpha Y(Z)} - \frac{H(Z=78)}{\sum_{Z=64}^{Z=68} H(Z)} \right|. \quad (5)$$

Only some of the halo stars have observations of platinum. So for the value of $H(Z = 78)$ we average only those halo stars in which this element has been observed.

To compare simulations to the solar r -process residuals, $N_{\odot,r}(A)$, we proceed in a similar fashion using the previous two constraints. As an additional, third, constraint we introduce and measure the amount of late-time neutron capture occurring in the rare earth region as these nuclides decay back to stability.

To gauge how close a simulation comes to reproducing the solar rare earth peak we use G_A^{REP} ,

$$G_A^{\text{REP}} \equiv \frac{\sum_{A=159}^{A=167} (\alpha Y(A) - N_{\odot,r}(A))^2}{\sum_{A=159}^{A=167} N_{\odot,r}(A)^2}. \quad (6)$$

In Equation (6), $Y(A) \equiv \sum_Z Y(Z, A)$ denotes the final abundance along an isobaric chain with atomic mass A and $N_{\odot,r}(A)$ is the solar r -process residual data also for an isobaric chain with atomic mass, A . Again, a lower value of G_A^{REP} implies a better match, with $G_A^{\text{REP}} = 0$ representing perfect agreement with $N_{\odot,r}(A)$. The final abundance pattern, $Y(A)$, from simulation is scaled individually by α which is the solution to $dG_A^{\text{REP}}/d\alpha = 0$.

Elemental abundance data from halo stars exhibit an $A = 195$ peak to rare earth peak ratio in agreement with the solar elemental abundance distribution. We thus use η_A , the ratio of the two peak heights for solar data as well,

$$\eta_A \equiv \left| \frac{\sum_{A=190}^{A=200} \alpha Y(A)}{\sum_{A=159}^{A=167} \alpha Y(A)} - \frac{\sum_{A=190}^{A=200} N_{\odot,r}(A)}{\sum_{A=159}^{A=167} N_{\odot,r}(A)} \right|. \quad (7)$$

Our third constraint comes from the observation that too much neutron capture during freezeout has negative consequences for the final r -process abundances (Arcones & Martínez-Pinedo 2011; Mumpower et al. 2011). This is particularly important for the rare earth region because the neutron capture rates in this region are on average faster than in other regions during the last stage of the r -process (Arcones & Martínez-Pinedo 2011; Mumpower et al. 2011). Late-time neutron capture effect shifts material from below the peak ($A = 150$ to $A = 158$) to above the peak ($A = 168$ to $A = 180$) causing an over production of the heavier rare earth elements, which does not resemble either the solar r -process residuals or halo star observations.

We contrast the abundances of two simulations to exhibit the late-time neutron capture effect in Figure 3. In both panels of the figure we show a snapshot of abundances at different points during the calculation. The top panel shows abundances at $R = 1$ (see point A, Figure 1), the middle panel shows abundances during freezeout (in between points B and C, Figure 1), and the bottom panel shows the final isotopic abundances as compared to the solar abundances. The peak forms successfully in both cases, panel (a) with conditions ($n = 6.0$, $S = 350k_B$, $Y_e = 0.30$) and panel (b) with conditions ($n = 2.0$, $S = 350k_B$, $Y_e = 0.30$). However, comparing the middle and bottom snapshots in panel (a) we can clearly see the late-time neutron capture effect during freezeout. This effect is not present when comparing the same snapshots in panel (b). One can also compare the differences in the free neutron abundance of these evolutions in Figure 2.

The late-time neutron capture effect is especially useful because, as we have just shown, it is also highly dependent on the conditions at late times. We thus can use this effect as a constraint on favorable r -process conditions. To estimate the amount of late-time neutron capture that shifts material across the rare earth region, we compute the difference between the value of G_A during freezeout (between points B and C on the

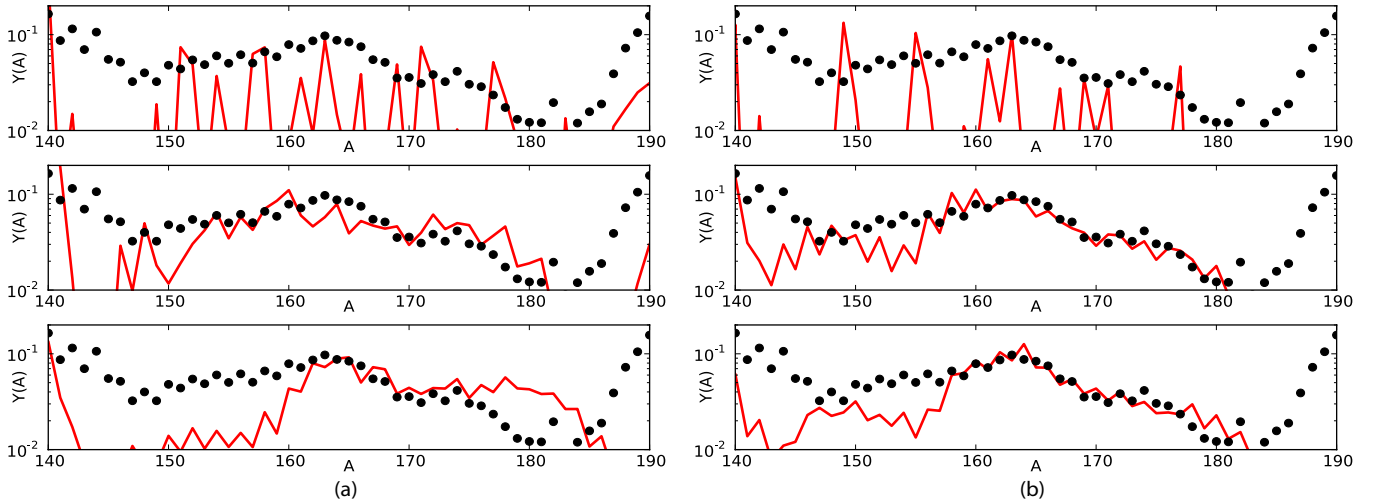


Figure 3. Highlights the late-time neutron capture effect by showing the time evolution of rare earth region abundances vs. the solar r -process curve (black) at three snapshots during the simulation. Panel (a) shows an r -process where late-time neutron capture occurs using conditions ($n = 6.0$, $S = 350k_B$, $Y_e = 0.30$). Panel (b) shows little to no late-time neutron capture using conditions ($n = 2.0$, $S = 350k_B$, $Y_e = 0.30$). Calculations were performed with the FRDM nuclear data. Abundances in the top row are shown at $R = 1$. Abundances in the middle row are shown in between $R = 1$ and the point at which β -decays take over. The bottom row shows final abundances. Refer back to Figure 1.

(A color version of this figure is available in the online journal.)

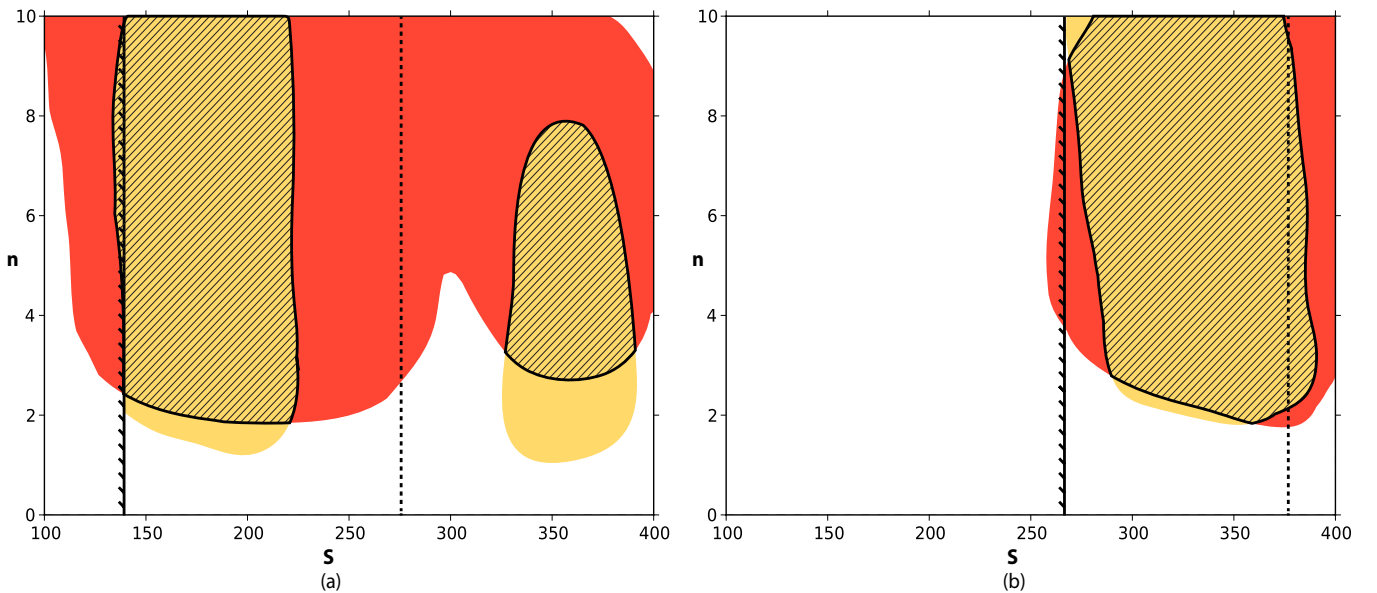


Figure 4. Shows how the rare earth region can be used to constrain astrophysical conditions when comparing simulations to typical halo star data. Calculations were performed with $Y_e = 0.30$, panel (a) and $Y_e = 0.40$, panel (b). The dark contour (red online) highlights conditions that produce a rare earth peak that best matches the average of five halo stars, $H(Z)$. The light contour (yellow online) highlights conditions that produce an $A = 195$ peak to rare earth peak that best matches $H(Z)$. The intersection of these constraints is showing by the hatching. A full r -process out to $A \sim 200$ occurs above entropies denoted by the solid vertical line. Above the dotted line fission influences the abundances of $A \gtrsim 150$ nuclides.

(A color version of this figure is available in the online journal.)

timeline) and the value of G_A using the final abundances. The summation now occurs over all rare earth elements ($A = 150$ to $A = 180$) signified by the superscript “REE:”

$$\Delta G_A^{\text{REE}} \equiv G_A^{\text{REE}}(\text{final}) - G_A^{\text{REE}}(\text{freezeout}). \quad (8)$$

3.2. Determining Freezeout Conditions

In Figure 4, we highlight astrophysical conditions where simulations best match $H(Z)$. The power law (n) from the density parameterization is plotted on the y -axis along with

entropy per baryon (S) on the x -axis. Panel (a) simulations have $Y_e = 0.30$ and panel (b) simulations have $Y_e = 0.40$. Shown in each panel is a solid vertical line which denotes the point at which a sufficient neutron-to-seed ratio ($R \sim 80$ at $T_9 \sim 3$) has been reached to produce a full r -process with elements out to $A \sim 200$ (Hoffman et al. 1997; Meyer & Brown 1997; Thompson et al. 2001). We also denote the point at which fission cycling influences the final abundances of the $A \gtrsim 150$ region by a dotted vertical line.

In Figure 5, we highlight astrophysical conditions where simulations best match $N_{\odot,r}(A)$. The axes and markings are the same as in Figure 4. The left column shows regions of

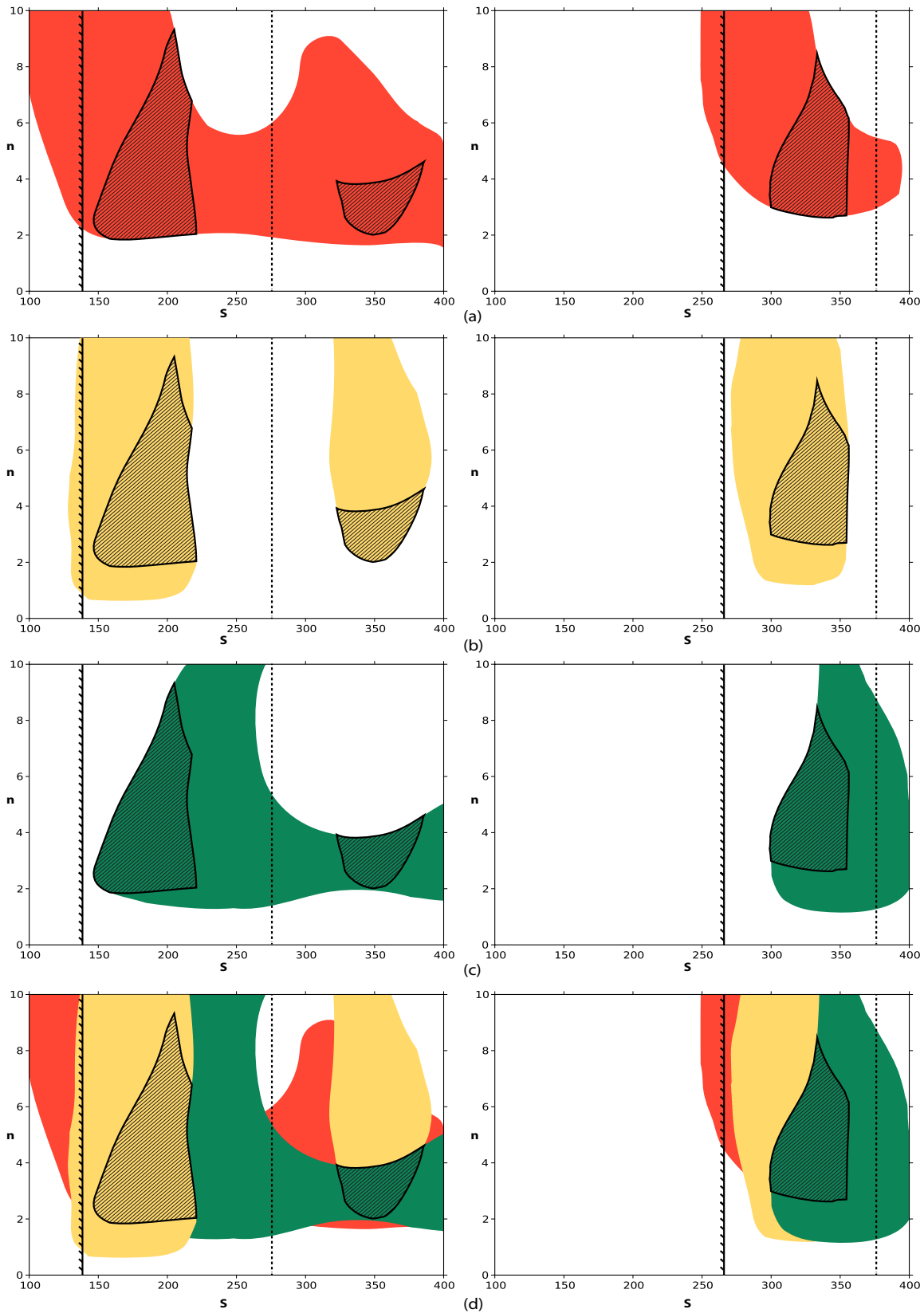


Figure 5. Shows how the rare earth peak can be used to constrain astrophysical conditions when comparing simulations to the solar r -process data. The axes are the same as Figure 4. The left column displays computations performed with $Y_e = 0.30$ and right column with $Y_e = 0.40$. Panel (a) highlights regions (red online) where the rare earth peak elements $A = 159$ to $A = 167$ from simulations best agree with the rare earth peak elements of the solar r -process data. Panel (b) shows regions (yellow online) where simulations produce the same ratio of the $A = 195$ peak to rare earth peak as compared to the solar data. Panel (c) highlights regions (green online) where the late-time neutron capture effect is minimal. The intersection (shaded region) of these three constraints is highlighted in each panel and repeated in panel (d) with all three constraints. A full r -process out to $A \sim 200$ occurs above entropies denoted by the solid vertical line. Above the dotted line fission influences the abundances of $A \gtrsim 150$ nuclides.

(A color version of this figure is available in the online journal.)

parameter space calculated with $Y_e = 0.30$ and the right column with $Y_e = 0.40$.

We now discuss below each of the abundance features individually and their impact on constraining freezeout conditions when comparing to halo star and solar data.

3.2.1. Using Rare Earth Peak Formation

Shown in both panels of Figure 4 is a dark shaded region (red online) where the scaled final abundances of rare earth peak elements from simulations best agree with the abundances of rare earth peak elements of $H(Z)$. Since no single simulation exactly reproduces the $H(Z)$ abundances, we must compute an appropriate cutoff for G_Z^{REP} . To this end, we measure the variance among the nuclear models by computing the standard deviation of the individual abundances at each value of $Y(Z)$ given constant conditions (n , S , Y_e). We additionally estimate the uncertainty in astrophysical environment by computing a second average over the simulations. Propagation of error from averaging the nuclear models and averaging over astrophysical conditions produces a value of $G_Z^{\text{REP}} = 0.03$. We thus take this value as a cutoff for shading the contour.

Shown in both columns of panel (a) of Figure 5 is a dark shaded region (red online) where the scaled final abundances of rare earth peak elements from simulations best agree with the abundances of rare earth peak elements of $N_{\odot,r}(A)$. We repeat the same procedure as mentioned above to compute the cutoff value of $G_A^{\text{REP}} = 0.15$ for shading this contour.

Fission during freezeout operates under higher entropy components ($S > 200k_B$ for $Y_e = 0.30$ and $S > 300k_B$ for $Y_e = 0.40$) and influences abundances at or above the rare earth region at $S \sim 275k_B$ for $Y_e = 0.30$ and $S \sim 375k_B$ for $Y_e = 0.40$. We denote the point at which fission is influential in both Figures 4 and 5 by a dotted line in each case. Without fission, the dark shaded contour would end at or before the dotted line. As can be seen from the figures, the inclusion of fission extends the favorable calculated freezeout conditions for rare earth peak formation.

3.2.2. Using the $A=195$ Peak to Rare Earth Peak Ratio

The light shaded region (yellow online) in both panels of Figure 4 represents the parameter space in which simulations produce the same ratio of the $A = 195$ peak to rare earth peak as compared to the averaged halo star, $H(Z)$. We take as an upper bound to this contour, $\eta_Z = 2$, which represents an over production of the $A = 195$ peak relative to the rare earth peak by a factor of two, the value of $\eta_Z \approx 2$ comes from the ratio $H(Z = 78) / \sum_{Z=64}^{Z=68} H(Z)$. We note that the under production of the $A = 195$ peak is taken care of by the sufficient neutron-to-seed ratio constraint (solid vertical line). All together, this results in a constraint similar to the method used by Meyer & Brown (1997). Qualitatively similar behavior is shown in the left and right columns of panel (b) of Figure 5, where calculated final abundances are compared to solar data. We take as an upper bound to this contour, $\eta_A = 4$, which again represents an over production of the $A = 195$ peak relative to the rare earth peak by approximately a factor of two.

Interestingly, the left columns of both figures, those with $Y_e = 0.30$, show a second favorable region for this ratio at higher entropy. This is due to the oscillation of the $A = 195$ peak as a function of R due to fission cycling as discussed in Beun et al. (2006, 2008). In the gap between the two favorable regions the $A = 195$ peak is over produced by more than a

factor of two compared to the rare earth peak. This effect also occurs in the $Y_e = 0.40$ case, however our simulations stop at $S = 400k_B$ and so the effect is not shown.

3.2.3. Using the Late-time Neutron Capture Effect

Returning to panel (c) of Figure 5, the shaded region (green online) in both columns represents the region of parameter space in which simulations do not exhibit a late-time neutron capture effect. We take as an upper bound to this contour, $\Delta G_A^{\text{REE}} = 1$, which represents significant fluctuations occurring across the rare earth region during freezeout.

Inspection of panel (c) reveals that the late-time neutron capture effect is sensitive to freezeout conditions, this is particularly evident at high entropy in the left column with $Y_e = 0.30$. During a cold freezeout (large values of n) the path moves far from stability where β -delayed neutron probabilities are large. As the nuclides decay back to stability, β -delayed neutron reactions provide an ample supply of neutrons for capture, see, e.g., the free neutron abundances in Figure 2. Additionally, fission actively introduces new seed nuclei into the region. Hence, the late-time neutron capture effect returns in this section of the figure causing the shaded contour to disappear. At high entropy, in a hot freezeout (lower values of n), the late-time neutron capture effect does not occur (presence of the shaded region) due to the presence of photodissociation and prolonged $(n, \gamma) \rightleftharpoons (\gamma, n)$ equilibrium.

3.3. Further Analysis

In order to emphasize the differences between the classical neutron-to-seed ratio constraint (the region of parameter space above the solid vertical line) and constraints using the rare earth elements, we highlight in each panel of Figures 4 and 5 a hatched region that represents our final constraint.

In Figure 4, where simulations are compared with halo star data, the final constraint region is generally controlled by the $A = 195$ peak to rare-earth-peak ratio as the rare earth peak formation alone is a less stringent constraint. In Figure 5, where simulations are compared with solar data, the final constraint region is generally controlled by the same peak height ratio and additionally the late-time neutron capture effect.

When comparing to both meteoritic and observational data given an initial $Y_e = 0.30$, we find the entropy range favorable for rare earth peak formation is $S \sim 150k_B$ to $S \sim 200k_B$ without fission. While the rare earth peak is formed by two different mechanisms in this entropy range, it does not favor one mechanism over the other. With the inclusion of fission a second favorable region appears around $S \sim 325k_B$ to $S \sim 375k_B$ in both figures. In this region, the rare earth peak formation and peak height constraints rule out the warmest and coldest scenarios when comparing to halo star data. When comparing to halo star data at high entropy, hot conditions are disfavored due to the constraint on the rare earth peak elements and colder conditions are disfavored because the $A = 195$ peak becomes over produced. When comparing to solar data, the late-time neutron capture effect rules out colder freezeout scenarios (see discussion in previous section).

We now explicitly investigate final abundances in the $Y_e = 0.30$ case to the halo star and solar data. In order to observe the abundance pattern that is typical of the region suggested by the new constraint procedure we average the final abundances in the constrained region and compute the standard deviation to measure the variance of these final abundances.

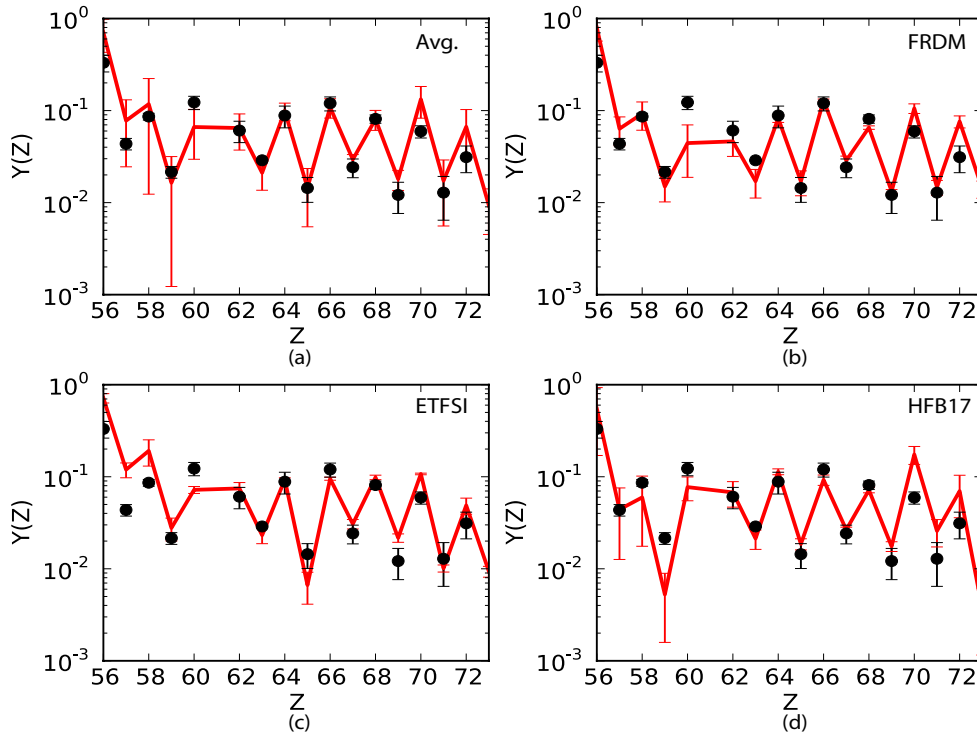


Figure 6. Shows calculated final averaged elemental abundance patterns (solid red) along with uncertainties compared to the average of five halo stars, $H(Z)$ (dots). All calculations were performed with $Y_e = 0.30$. Panel (a) shows an average over three nuclear data sets and astrophysical conditions from the constraint region of Figure 4. Panels (b)–(d) show the average over astrophysical conditions in the constraint region for each individual nuclear model.

(A color version of this figure is available in the online journal.)

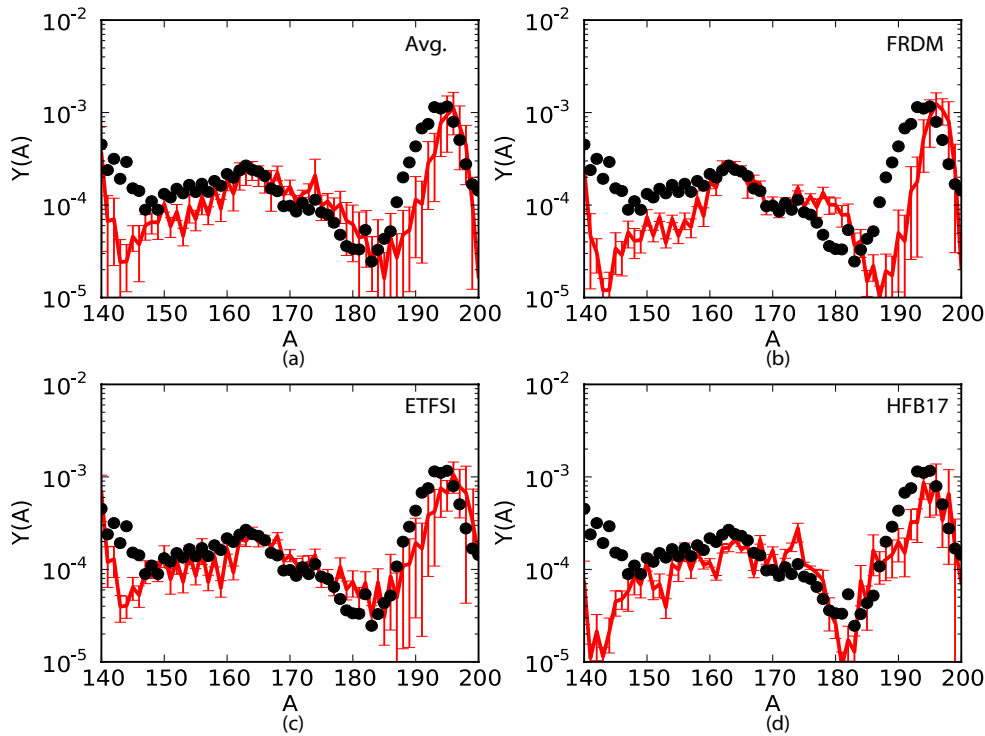


Figure 7. Shows calculated final averaged isotopic abundance patterns (solid red) along with uncertainties compared to the solar r -process residuals (black dots). All calculations were performed with $Y_e = 0.30$. Panel (a) shows the average over three nuclear data sets and astrophysical conditions from the constraint region of Figure 5. Panels (b)–(d) show the average over astrophysical conditions in the constraint region for each individual nuclear model.

(A color version of this figure is available in the online journal.)

The results of these calculations are shown in Figures 6 and 7. Panel (a) includes both averages over nuclear physics data sets and astrophysical conditions and the error bars represent

variance from nuclear models and astrophysical conditions. The abundances in panel (a) correspond with simulations in the hatched region of the left column of Figures 4 and 5, respectively.

Panels (b)–(d) show the final abundances of individual nuclear models after averaging over their respective constraint regions and the error bars represent the variance from astrophysical conditions alone.

As can be seen from Figure 6, these simulations do very well in reproducing the rare earth peak. When comparing to $H(Z)$, the largest variation in the rare earth peak region comes from terbium, $Z = 65$. Among all of the lanthanides, praseodymium, $Z = 59$, shows the largest variance while neodymium, $Z = 60$, is consistently under produced. Figure 7 also shows similar results for the rare earth peak elements. When comparing to the solar data, the largest variances in the final abundances can be found in the $A \sim 180$ to $A \sim 195$ region. This effect has been suggested to arise from a lack of long range correlations in the nuclear models (Arcones & Bertsch 2011).

It is important to note in both figures that the variance seen in the final abundances of the rare earth elements is small. While subtleties persist in the individual nuclear models, global trends consistent with halo star and solar abundances distribution are present. As expected, we isolate conditions where the rare earth peak and the solar $A = 195$ to rare earth peak ratio mimic the solar data and further prevent too much build up of the heavier rare earths.

The method presented here only relies upon the input nuclear physics and r -process observables and so is sufficiently general as to be applied to other nucleosynthesis environments. Suitable conditions for production of rare earth nuclei are found in neutron star mergers, however current models in the literature do not show a rare earth peak (Goriely et al. 2005; Arnould et al. 2007; Goriely 2011). These models suggest that the peak temperature is on the order of $T_9 \approx .5$, so if rare earth peak formation were to occur it would be from one or possibly a combination of mechanisms (1) and (3) mentioned in Section 1. In the decompression of initially cold neutron star matter, the nuclear flow proceeds for some time along the dripline so the details of nucleosynthesis are subject to large nuclear physics uncertainties stemming from the model-dependent properties of these nuclei as well as fission probabilities and fragment distributions. These substantial uncertainties in nuclear physics would influence the suitable limits of G_Z^{REP} and G_A^{REP} . Thus, as with any environment, the success of the method is clearly dependent on how well we understand the input nuclear physics.

Recent observations of tellurium ($Z = 52$) have been made by Roederer et al. (2012) in several halo stars which show the $A = 130$ peak element in agreement with the elemental abundances of the same region in the solar pattern. This observation suggests that $A = 130$ elements may be produced in the same sort of environment as the rare earth and heavier elements. We have included these new observations in our calculations in order to compute the $A = 130$ to rare earth peak ratio for comparison of elemental abundances. In the context of our calculations the region of astrophysical parameter space where this ratio matches both elemental and isotopic data is consistently small. This suggests that the $A = 130$ peak may be produced under different conditions than that of the rare earth or $A = 195$ peaks or the $A = 130$ peak may be produced by a combination of weak and main r -process components. However, a word of caution is warranted: Nucleosynthesis calculations of the $A = 130$ peak are complicated since the peak is sensitive to the relative strength of β -decay rates and the details of fission fragment distributions. Thus, further investigation is needed regarding both of these points.

4. SUMMARY AND CONCLUSIONS

Using the delicate, out of $(n, \gamma) \rightleftharpoons (\gamma, n)$ equilibrium formation process of the rare earth peak we have studied and isolated freezeout conditions in high-entropy ($S \gtrsim 100k_B$) r -process calculations conducive for production of these elements. We compare the final abundances from simulations to both the elemental abundances of halo stars and the isotopic abundances of the solar r -process residuals. Both of these data sets suggest similar astrophysical conditions during freezeout. For example, without fission, we find that favorable freezeout conditions fall within a narrow entropy window ($S \sim 150k_B$ to $S \sim 200k_B$) given an initial electron fraction, $Y_e = 0.30$ and timescale of $\tau \sim 27$ ms. Given an initial electron fraction, $Y_e = 0.40$ and same initial timescale we find an entropy window of $S \sim 300k_B$ to $S \sim 350k_B$.

The sensitivity of final abundances to uncertainties in nuclear physics is considered by including calculations with the FRDM, ETFSI, and HFB-17 nuclear models. We consider the variance among final abundances due to these three models and include it when determining the appropriate constraint for the formation of the rare earth peak (values of G_Z^{REP} and G_A^{REP}).

We use three abundance features to constrain astrophysical conditions: (1) We require the formation and correct shape of the rare earth peak ($A = 157$ to $A = 167$ or $Z = 64$ to $Z = 68$). The importance of this process and its sensitivity to freezeout conditions was discussed in Mumpower et al. (2011). (2) We utilize the constraint on the ratio of the abundance in the rare earth peak to that of the $A = 195$ peak, as these elements are believed to be synthesized in the same environment. (3) We utilize a new constraint on freezeout behavior: the late-time neutron capture constraint.

The late-time neutron capture constraint involves studying the shifting of material between isotopes during freezeout in the rare earth region. We find the over production of the heaviest rare earth elements is highly dependent on the conditions during freezeout, making it a valuable consideration for r -process models. This effect can be measured by comparing abundances to solar r -process residuals as this data provides isotopic information.

The impact of fission during freezeout is to produce multiple islands of favorable r -process conditions, see, e.g., the left column of Figures 4 or 5. The late-time neutron capture constraint becomes tighter when fission occurs. This is due to two factors: (1) a cold r -process freezeout extends far from stability where β -delayed neutron probabilities are large, providing additional free neutrons to capture during freezeout. (2) The inclusion of fission during freezeout cycles additional material through the rare earth region which can capture the free neutrons. This suggests that if fission is important for the formation of the r -process elements, the astrophysical freezeout conditions are more likely to be “hot.”

We have shown that the formation of the rare earth peak is a useful tool in determining favorable high-entropy ($S \gtrsim 100k_B$) r -process freezeout conditions. This diagnostic works well despite current uncertainties in nuclear physics. It complements the commonly used neutron-to-seed ratio and should be used in addition when analyzing astrophysical models. The size of the range of acceptable astrophysical conditions is dominated by uncertainty in the nuclear physics inputs. Reduction of this uncertainty through an improved understanding of the properties of nuclei far from stability and self-consistent nuclear data will increase the efficacy of this tool.

We thank Raph Hix for providing the charged particle network and up-to-date reaction libraries. We also thank North Carolina State University for providing the high performance computational resources necessary for this project. This work was supported in part by U.S. DOE Grant No. DE-FG02-02ER41216, DE-SC0004786, and DE-FG02-05ER41398.

REFERENCES

- Arcones, A., & Bertsch, G. 2011, *Phys. Rev. Lett.*, **108**, 151101
- Arcones, A., & Martínez-Pinedo, G. 2011, *Phys. Rev. C*, **83**, 4
- Arlandini, C., Kappeler, F., Wisshak, K., et al. 1999, *ApJ*, **525**, 886
- Arnould, M., Goriely, S., & Takahashi, K. 2007, *Phys. Rep.*, **450**, 97
- Banerjee, P., Haxton, W., & Qian, Y. 2011, *Phys. Rev. Lett.*, **106**, 20104
- Baruah, S., Audi, G., Blaum, K., et al. 2008, *Phys. Rev. Lett.*, **101**, 26
- Beun, J., McLaughlin, G., Surman, R., & Hix, W. 2006, in Proc. Int. Symp. on Nuclear Astrophysics, Nuclei in the Cosmos IX (Trieste: Proceedings of Science), **140**
- Beun, J., McLaughlin, G., Surman, R., & Hix, W. 2008, *Phys. Rev. C*, **77**, 3
- Burbidge, E., Burbidge, G., Fowler, W., & Hoyle, F. 1957, *Rev. Mod. Phys.*, **29**, 547
- Cameron, A. 1957, *PASP*, **69**, 201
- Cowan, J., McWilliam, A., Sneden, C., & Burris, D. 1997, *ApJ*, **480**, 246
- Cowan, J., & Sneden, C. 2006, *Nature*, **440**, 1151
- Cowan, J., Sneden, C., Burles, S., et al. 2002, *ApJ*, **572**, 861
- Freiburghaus, C., Rembges, J., Rauscher, T., et al. 1999, *ApJ*, **516**, 381
- Grawe, H., Langanke, K., & Martínez-Pinedo, G. 2007, *Rep. Prog. Phys.*, **70**, 1525
- Goriely, S., Bauswein, A., & Janka, H. 2011, *ApJ*, **738**, L32
- Goriely, S., Chamel, N., & Pearson, J. 2008, *A&A*, **487**, 767
- Goriely, S., Chamel, N., & Pearson, J. 2009, *Phys. Rev. Lett.*, **102**, 152503
- Goriely, S., Demetriou, P., Janka, H., Pearson, J., & Samyn, M. 2005, *Nucl. Phys. A*, **758**, 587
- Hill, V., Plez, B., Cayrel, R., et al. 2002, *A&A*, **387**, 560
- Hix, W., & Thielemann, F. 1999, *Comput. Appl. Math.*, **109**, 321
- Hoffman, B., Woosley, S., & Qian, Y. 1997, *ApJ*, **482**, 951
- Hosmer, P., Schatz, H., Aprahamian, A., et al. 2005, *Phys. Rev. Lett.*, **94**, 112501
- Hosmer, P., Schatz, H., Aprahamian, A., et al. 2010, *Phys. Rev. C*, **82**, 025806
- Ivans, I., Simmerer, J., Sneden, C., et al. 2006, *ApJ*, **645**, 613
- Jones, K., Pain, S., Kozub, R., et al. 2009, in AIP Conf. Proc. 1098, FUSION08: New Aspects of Heavy Ion Collisions Near the Coulomb Barrier, ed. K. E. Rehm et al. (Melville, NY: AIP), **153**
- Kappeler, F., Beer, H., & Wisshak, K. 1989, *Rep. Prog. Phys.*, **52**, 945
- Lattimer, J., Mackie, F., Ravenhall, D., & Schramm, D. 1977, *ApJ*, **213**, 225
- Lodders, K., Palmee, H., & Gail, H. 2009, arXiv:0901.1149
- Marti, K., & Zeh, H. 1985, *Meteoritics*, **20**, 311
- Matoš, M., Estrade, A., Amthor, M., et al. 2008, *J. Phys. G Nucl. Part. Phys.*, **35**, 014045
- McLaughlin, G., & Surman, R. 2005, *Nucl. Phys. A*, **758**, 189
- Metzger, B., et al. 2010, *MNRAS*, **406**, 2650
- Meyer, B. 1989, *ApJ*, **343**, 254
- Meyer, B. 2002, *Phys. Rev. Lett.*, **89**, 231101
- Meyer, B., & Brown, J. 1997, *ApJS*, **112**, 199
- Meyer, B., Mathews, G., Howard, W., Woosley, S., & Hoffman, R. 1992, *ApJ*, **399**, 656
- Möller, P., Nix, J., Myers, W., & Swiatecki, W. 1995, *At. Data Nucl. Data Tables*, **59**, 185
- Möller, P., Pfeiffer, B., & Kratz, K. 2003, *Phys. Rev. C*, **67**, 055802
- Mumpower, M., McLaughlin, G., & Surman, R. 2010, in Proc. Int. Sym. on Nuclear Astrophysics, Nuclei in the Cosmos XI (Trieste: Proceedings of Science), **273**
- Mumpower, M., McLaughlin, G., & Surman, R. 2011, *Phys. Rev. C*, **85**, 045801
- Quinn, M., Aprahamian, A., Pereira, J., et al. 2011, *Phys. Rev. Lett.*, **106**, 052502
- Otsuki, K., Mathews, G., & Kajino, T. 2003, *New Astron.*, **8**, 767
- Panov, I., & Janka, H. 2009, *A&A*, **494**, 829
- Pearson, J., Nayak, R., & Goriely, S. 1996, *Phys. Lett. B*, **387**, 455
- Quinn, M., Aprahamian, A., Pereira, J., et al. 2011, *Phys. Rev. C*, **85**, 035807
- Qian, Y., & Wasserburg, G. 2007, *Phys. Rep.*, **442**, 237
- Qian, Y., & Woosley, S. 1996, *ApJ*, **471**, 331
- Rahaman, S., Elomaa, V., Eronen, T., et al. 2008, *Acta Phys. Pol. B*, **39**, 463
- Rauscher, T., & Thielemann, F. 1998, arXiv:nucl-th/9802040
- Rauscher, T., & Thielemann, F. 2000, *At. Data Nucl. Data Tables*, **75**, 1
- Roederer, I., Cowan, J., Karakas, A., et al. 2010, *ApJ*, **724**, 975
- Roederer, I., Lawler, J., Cowan, J., et al. 2012, *ApJ*, **747**, 1
- Seeger, P., Fowler, W., & Clayton, D. 1965, *ApJS*, **11**, 121
- Schenk, O., & Gärtner, K. 2004, *Future Gener. Comput. Syst.*, **20**, 475
- Schramm, D., & Fowler, W. 1971, *Nature*, **231**, 103
- Sneden, C., Cowan, J., & Gallino, R. 2008, *ARA&A*, **46**, 241
- Sneden, C., McWilliam, A., Preston, G., et al. 1996, *ApJ*, **467**, 819
- Suess, H., & Urey, H. 1956, *Rev. Mod. Phys.*, **28**, 53
- Sumiyoshi, K., Suzuki, H., Otsuki, K., Terasawa, M., & Yamada, S. 2000, *PASJ*, **52**, 601
- Surman, R., Beun, J., McLaughlin, G., & Hix, W. 2009, *Phys. Rev. C*, **79**, 4
- Surman, R., & Engel, J. 2001, *Phys. Rev. C*, **64**, 3
- Surman, R., Engel, J., Jonathan, R., & Meyer, B. 1997, *Phys. Rev. Lett.*, **79**, 1809
- Surman, R., & McLaughlin, G. 2004, *ApJ*, **603**, 611
- Surman, R., McLaughlin, G., & Hix, W. 2006, *ApJ*, **643**, 1057
- Surman, R., McLaughlin, G., Ruffert, M., Janka, H., & Hix, W. 2008, *ApJ*, **679**, L117
- Suzuki, T., Yoshida, T., Kajino, T., & Otsuka, T. 2012, *Phys. Rev. C*, **85**, 1
- Thompson, T., Burrows, A., & Meyer, B. 2001, *ApJ*, **562**, 887
- Wanajo, S. 2007, *ApJ*, **666**, L77
- Westin, J., Sneden, C., Gustafsson, B., & Cowan, J. 2000, *ApJ*, **530**, 783
- Woosley, S., Hartmann, D., Hoffman, R., & Haxton, W. 1990, *ApJ*, **356**, 272